Level crossings reveal organized coherent structures in a turbulent time series

Subharthi Chowdhuri * and Tirtha Banerjee
Department of Civil and Environmental Engineering, University of California, Irvine, California 92697, USA

(Received 29 August 2023; accepted 21 December 2023; published 17 January 2024)

In turbulent flows, energy production is associated with highly organized structures, known as coherent structures. Since these structures are three dimensional, their detection remains challenging in the most common situation in experiments, when single-point temporal measurements are considered. While previous research on coherent structure detection from time series employs a thresholding approach, either in spectral or temporal domain, the thresholds are ad hoc and vary significantly from one study to another. To circumvent this issue, we introduce the level-crossing method and show how specific features of a turbulent time series associated with coherent structures can be objectively identified, without assigning *a priori* any arbitrary threshold. By using two wall-bounded turbulence time-series datasets (at a Reynolds number of 10^4), we successfully extract through level-crossing analysis the impacts of coherent structures on turbulent dynamics and therefore open an alternative avenue in experimental turbulence research. By utilizing this framework further, we discover a metric, characterized by a statistical asymmetry between the peaks and troughs of a turbulent signal, to quantify inner-outer interaction in wall turbulence. Most importantly, through phase-randomized surrogate data modeling, we demonstrate that the level-crossing statistics are quite sensitive to the nonlinear dependencies in a turbulent signal. Physically, this finding implies that the large-scale coherent structures modulate the near-wall turbulent dynamics through a nonlinear interaction associated with low-speed streaks, a mechanism not identifiable from spectral analysis alone. Moreover, a connection is established between extreme value statistics and level-crossing analysis, thereby allowing additional possibilities to study extreme events in other dynamical systems.

DOI: 10.1103/PhysRevFluids.9.014601

I. INTRODUCTION

According to Hussain [1], coherent structures in turbulent flows are defined as "a connected large-scale turbulent fluid mass with a phase correlated vorticity over its spatial extent." However, while dealing with time-series measurements, this formal definition is not very useful since from temporal observations alone it is difficult to identify the organized patterns in the flow. Therefore, instead of rigorously defining the coherent structures, they can be best described by their phenomenology, such as (a) their characteristic scales are comparable to the integral scales [2–4], (b) they induce non-Gaussian fluctuations in the turbulent variables [5–7], and (c) they have large contributions to turbulent fluxes and kinetic energy [1,7,8]. Geometrically, these structures are three dimensional and can take various shapes based on the types of turbulent flow. Examples include granular patterns in astrophysical flows [9], hairpin structures in neutral wall-bounded flows [10], and counter-rotating roll vortices in atmospheric turbulence [11]. In addition to their significance in drag reduction [12], consideration of coherent structures is also important for weather and climate models since

*subharc@uci.edu

disregarding those can cause significant uncertainties in turbulence parametrization [13]. For the rest of the discussion, we focus our attention on wall-bounded turbulence, since such flows are ubiquitous in nature and the features of coherent structures in these flows are well established [8].

In practice, the coherent structures can be visually recognized from three-dimensional numerical simulations, smoke visualization experiments, or particle velocimetry measurements. Apart from their visual recognition, the coherent structures can also be reconstructed through proper orthogonal decomposition, a technique often applied to numerical simulations or particle velocimetry measurements [14]. Despite such advances, it remains challenging to detect them from the most common form of turbulent experiments where the variables are measured at a single point in time. Previous studies on coherent structure detection from turbulent time series employ a thresholding approach, where the thresholds are set either in the temporal or spectral domain. Interestingly, thresholding approach has also been employed to detect coherent structures from spatial measurements [15,16], although we will not discuss them here.

Regarding the spectral domain, the thresholds are set on the Fourier wave numbers to separate the coherent structures from small-scale turbulence. This concept mainly originated with the three-wave-number range model of the spectra of streamwise velocity fluctuations, introduced by Perry and Abell [17], Perry and Chong [18], and Perry and Li [19] (see Raupach *et al.* [20] for a review). These fluctuations were measured at a single point in time and the frequencies were converted to wave numbers (or, equivalently, the wavelengths) by applying Taylor's hypothesis. Taylor's hypothesis allows the frequencies to be interpreted as the spatial scales of the turbulent structures (measured by wave numbers) under the assumption that these structures pass over the measurement location with the local mean velocity [21]. Accordingly, in the three-wave-number range model, the low wave numbers with the wavelengths of the order of boundary layer height or radius of the pipe, represented the large-scale coherent structures. In the parlance of wall turbulence [3,22], these structures are named as large- and very large scale motions (LSMs and VLSMs). At intermediate wave numbers, the velocity spectra displayed a -1 spectral power law, which Perry and Chong [18] demonstrated to be related to Townsend's attached eddies whose sizes scaled with height. Last, the large wave numbers represented the eddies that populated the inertial subrange and dissipative range of the spectra.

All these three-wave-number ranges were empirically determined by assigning some cut-off numbers. Later, to learn more about coherent structures, spectral analysis was undertaken on the time-series measurements of streamwise velocity at multiple heights. By analyzing the premultiplied spectra, two distinct peaks were identified [21,23]. One of those peaks was located very close to the wall, representing the inner-layer structures often associated with bursting events. On the other hand, the second peak (also known as the outer-spectral peak) was located in the log layer, associated with the LSMs and VLSMs. A large body of literature on wall turbulence used this scale-separation information to decipher how the large-scale structures (LSMs and VLSMs) in the logarithmic region modulate the dynamics occurring in the layers below the log layer (commonly known as inner layer), a phenomenon referred to as inner-outer interaction [23–25].

The inner-outer interaction is usually quantified in the spectral domain with an amplitude modulation coefficient. The estimation of this coefficient involves several steps, as outlined by Mathis *et al.* [23] and Pathikonda and Christensen [26] and briefly summarized here. First, the large-scale signatures (representing the LSMs and VLSMs) are computed through filtering the velocity signal at a fixed point in the logarithmic layer by assigning a spectral cutoff at wavelengths comparable to the outer-spectral peak. Second, the small scales (representing the inner-layer structures) are identified as the high-pass-filtered velocity time traces at a point very close to the wall. Third, an envelope of the small-scale portion of the signal is estimated using a Hilbert transform and further filtered at a same cut-off scale of the outer-layer structures. Fourth, a correlation coefficient, otherwise known as the amplitude modulation coefficient, is computed between the filtered envelope of the small scales and the large-scale portion of the signal. Note that, although there exist a few studies that use a slightly different method to compute this inner-outer interaction, like performing a conditional statistical analysis based on the sign of a low-pass Fourier filtered velocity signal [25]

or using wavelets instead of Fourier analysis [27], the conclusions remain the same. For instance, while plotting the variations in the amplitude modulation coefficient with height, Mathis *et al.* [23] observed an interesting outcome. A high level of correlation was observed for the inner layer, which progressively decreased as the heights approached the log layer. Mathis *et al.* [23] interpreted this behavior as an evidence that the inner-layer turbulence dynamics was strongly modulated by low-wave-number motions associated with the log region, otherwise known as the outer region.

By contrast, in the temporal domain, thresholds are applied directly on the time series and historically were chosen in a manner so that the frequency of the detected structures matched with the smoke visualization experiments [28]. Since then, these temporal thresholds have been used extensively to deduce the impacts of outer-layer structures on near-wall turbulent bursts [29–31]. However, the thresholds to identify the bursts suffer from subjectivity as their values differ significantly from one study to another [32]. Additionally, the rationale behind their choices also varies, since some studies consider the thresholds where the probability density functions (PDFs) of the time series differ from a Gaussian, some assign arbitrary thresholds to the magnitude of streamwise velocity fluctuations, while others choose them from a quadrant perspective [33]. Akin to the temporal domain, the thresholds in the spectral domain too suffer from several pragmatic issues. First, the spectral thresholds often require information about certain external parameters (such as boundary layer height or free-stream velocity) whose measurements are not readily available for all flow types. Second, to achieve proper scale separation observations are needed at multiple heights, which are hard to obtain. Third, in the absence of external parameters or multipoint observations, the cut-off wavelengths to separate coherent structures become arbitrary and remain at the mercy of those conducting the analysis. To eliminate these difficulties, we introduce a level-crossing technique through which the coherent structures can be detected from time series without assigning a prior any tunable thresholds or external parameters.

Although a handful of previous research, such as the ones by Tardu and Bauer [34] and Poggi and Katul [35], have used level-crossing analysis to study the Reynolds stress production and dissipation of kinetic energy in wall turbulence, we demonstrate that this approach could be generalized further to detect coherent structures. In a level-crossing method [36], one seeks a statistical description of timescales $t_p|_\alpha$ (where the subscript p indicates persistence) up to which a stochastic variable $f(t)$ remains larger or smaller than $\overline{f} \pm (\alpha \times \sigma_f)$, where t is time, $\overline{f}$ is the temporal mean, σ_f is the standard deviation, and α is a given threshold. A brief review of level-crossing approach is provided by Friedrich *et al.* [37], which, in other words, is a generalization of the zero-crossing or persistence analysis where α level is set at zero [34,38]. For many different turbulent flows, the PDFs $[P(t_p|_{\alpha=0})]$ of $t_p|_{\alpha=0}$ are power laws with an exponential cutoff [39–41]. On the one hand, the exponential cutoff represents a Poisson distribution, associated with t_p values larger than the integral scales [42]. For practical purposes, the integral scales (γ_x, where x is any turbulent signal) are obtained by integrating the autocorrelation functions of x up to its first zero crossing and therefore have the units of time [43]. On the other hand, Blake and Lindsey [36] show that $P(t_p|_\alpha)$ becomes a Poisson distribution when α values are substantially large.

Several points are now considered. First, the Poisson distribution is associated with a stochastic process for which the autocorrelation function stays zero at all timescales [38]. Second, in a turbulent time series, the measurements become weakly correlated with each other at scales larger than the integral scales, since the autocorrelation functions drop to zero [42]. Third, the characteristic scales of coherent structures are comparable to the integral scales [2]. Fourth, in a randomly shuffled (RS) signal, the autocorrelation functions cease to exist [44]. By combining all these aspects, we hypothesize that the thresholds to detect coherent structures could be objectively determined as that particular α for which $P(t_p|_\alpha)$ of the original signal matches with its RS counterpart. Intrigued by this possibility, we ask the following: (1) By changing α what stochastic features of a turbulent time series are revealed?, (2) Do the detected coherent structures from the critical α value obey the flow physics?, and (3) Can we identify the organizational aspects of coherent structures through the level-crossing approach?

To address these research questions, in addition to the level-crossing analysis, we also employ event-synchronization analysis and surrogate data modeling. Unlike previous research, where the relationships between the two vertically separated points are studied through cross-correlation and spectral-coherence techniques [45,46], event-synchronization analysis quantifies how the positive and negative turbulent events occurring at two distant points (vertically separated) in a flow field are connected to each other. By doing so, we address the point whether the detected features from the level-crossing approach comply with the phenomenology of the coherent structures. On the other hand, surrogate data modeling is often employed to infer about the organizational aspects of coherent structures in turbulent flows [47–49]. Therefore, we borrow those techniques to explain the results obtained from level-crossing analysis. For our purposes, we use two hot-wire temporal datasets, collected from a zero-pressure-gradient turbulent boundary layer generated in the Melbourne wind tunnel [50]. These datasets have been used before [27,51,52] and are trustworthy. During our presentation, we arrange the article in three different sections. In Sec. II we provide brief descriptions of the experimental datasets and methodology, in Sec. III we introduce the results and discuss them, and, last, in Sec. IV we summarize the key takeaways and provide the scope for further research.

II. DATASET AND METHODOLOGY

Corresponding to both hot-wire datasets, the friction Reynolds numbers (Re) are of the order of 10^4, as illustrated in Baars *et al.* [27]. The wall-normal heights are normalized by friction velocity (u_*) and kinematic viscosity (ν) and denoted as $y^+ = yu_*/\nu$, where $^+$ refers to wall scaling. Of the two datasets, one was sampled at a frequency (f_s) of 20 kHz (T1 dataset) and the other at 44 kHz (T2 dataset). Note that for both datasets, one probe is fixed (reference probe) while the others traverse across heights (traveling probes) and remain synchronized with the reference probe at all times [27]. Moreover, for the T1 dataset, the time series of streamwise velocity was collected over three acquisition cycles, each with 120-s duration. Therefore, the results presented for the T1 dataset are ensemble averaged over these three measurement cycles. However, for the T2 dataset, only a single cycle of 360-s duration was used. Regarding our purposes, we consider the streamwise velocity fluctuations (u') after subtracting the temporal mean ($\overline{u}$). The turbulence statistics, such as the profiles of wall-normalized mean velocity ($\overline{u}/u_*$) and velocity variance (σ_u^2/u_*^2), compare well between the two datasets (see Fig. S1a in Ref. [53]). In accordance with previous findings, the zero-crossing PDFs [$P(t_p|_{\alpha=0})$] of T1 and T2 datasets, when normalized with the integral scales of u' (γ_u), follow a power-law distribution with an exponential cutoff (Fig. S1b). In this study γ_u is the integral scale of u', has a unit of time, and is obtained by integrating the autocorrelation function of u' up to its first zero crossing. Since the autocorrelation functions converge towards zero, the estimates of γ_u are robust. Subsequently, to gather more information on the coherent structures we apply level-crossing analysis, event-synchronization analysis, and surrogate data modeling whose rationale are discussed below one by one.

A. Level-crossing analysis

To demonstrate the philosophy behind level-crossing analysis, we use a segment of a u' time series (normalized by its standard deviation σ_u) from the T1 dataset at height $y^+ = 66.84$, whose timescale axis is scaled by the wall scaling such that $t^+ = tu_*^2/\nu$ [Fig. 1(a)]. Corresponding to this time series, one can generate its telegraphic approximations (TA) by denoting the values above a threshold to be 1 and 0 otherwise [54,55]. In the bottom panels of Fig. 1(a), we show three TA sequences at threshold levels $\alpha = 0, 2, -2$. One can clearly see as the threshold levels are increased, the timescales $t_p|_\alpha$ of the TA patterns become substantially large. In fact, if $t_p|_\alpha$ values become comparable to the integral scales of u' (γ_u), then one would expect the TA patterns associated with those α levels to resemble a random configuration.

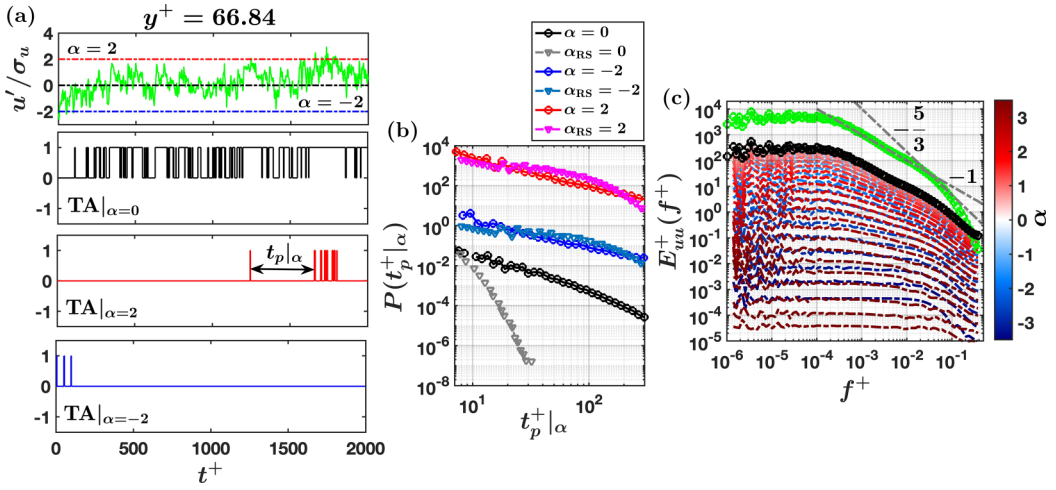

FIG. 1. (a) A segment of u' time series and its telegraphic approximations (TA) at different threshold levels (α) are shown from $y^+ = 66.84$ of T1 dataset. The u' values are scaled by σ_u while the time axis (t^+) is normalized by the wall units. The level-crossing timescales at different α values are denoted as $t_p|_\alpha$. (b) For the same segment of the u' time series, the PDFs of $t_p^+|_\alpha$ are shown for $\alpha, \alpha_{RS} = 0, 2, -2$, corresponding to the original and randomly shuffled (RS) signals. Note that α_{RS} values indicate the thresholds for RS signals. For visual purposes, $P(t_p^+|_\alpha)$ of original and its RS counterparts at $\alpha, \alpha_{RS} = 2, -2$ levels are shifted vertically upwards. (c) The energy spectrum of the time series at $y^+ = 66.84$ is compared with the TA series at different α levels in an interval of 0.2. The thick black line with circular markers indicates the TA spectrum at $\alpha = 0$ level. The power laws -1 and $-5/3$ are shown in dash-dotted gray lines. The frequencies (f^+) and spectral energy densities (E_{uu}^+) are normalized by the wall scalings.

This indeed appears to be the case when one compares the PDFs of the level-crossing timescales for the three α values between the original and RS signals [Fig. 1(b)]. Before plotting their PDFs, the level-crossing timescales are scaled by the wall scaling and denoted as $t_p^+|_\alpha$. The α values corresponding to the RS signals are denoted as α_{RS}. For the ease of visualization, in Fig. 1(b), the PDFs [$P(t_p^+|_\alpha)$] of original and its RS counterparts at $\alpha, \alpha_{RS} = 2, -2$ levels are shifted vertically upwards. As opposed to $\alpha = 0$, for $\alpha = 2, -2$, $P(t_p^+|_\alpha)$ of u' signal has an excellent agreement with its RS counterpart. This can be confirmed through the q-q plots, where the $t_p|_\alpha$ values between the original and RS signals follow a straight line with 45° slope for $\alpha = -2, 2$, thereby indicating that they are both sampled from similar distributions (not shown here).

The apparent randomness in $t_p|_\alpha$ at large α values can be further investigated by showing how the energy spectrum of the TA patterns change as α is varied systematically. For both wall-bounded engineering and atmospheric flows, Sreenivasan and Bershadskii [54] and Cava *et al.* [42] showed that the energy spectrum of the TA patterns corresponding to $\alpha = 0$ level, preserve the information about the spectral power laws, despite the fact that the TA sequences do not contain any amplitude information. In Fig. 1(c) we show the energy spectra of the TA patterns with different α values and compare the same with the original u' signal at $y^+ = 66.84$ (green line with circular markers). Note that the frequencies (f^+) and spectral energy densities (E_{uu}^+) in Fig. 1(c) are normalized with the wall scalings. One can see that at $\alpha = 0$ level (black line with circles), the energy spectrum shows a -1 spectral scaling at smaller frequencies similar to the original signal, but at larger frequencies the $-5/3$ scaling law appears to be a little different. Since the TA patterns do not contain any amplitude information, their spectral energies appear attenuated as compared to the original, but the overall trend remains similar. However, at large-enough α values (indicated by deep red or blue colors for the positive or negative sides), the scaling laws disappear from the TA energy spectra and they nearly attain a flat shape as expected for a random signal. This information is utilized in Sec. III A,

where we show by increasing α a critical value is reached, using which one could study certain flow features whose characteristic scales are comparable to γ_u.

B. Event-synchronization analysis

By conducting an event-synchronization analysis, one seeks to describe how the positive and negative patterns (with respect to $\alpha = 0$ level) in a turbulent signal are coupled with each other across different wall-normal heights. This information is important to establish how the nonlocal influences impact the organization of turbulent events in wall-bounded flows.

For event synchronization analysis, we consider a joint distribution between the positive and negative patterns corresponding to the velocity signals from the reference probe (u'_{ref}) and from a traveling probe situated at any particular height (u'). For T1 dataset, the reference probe is located at $y^+ = 4.3$, while for T2 it is at $y^+ = 474$ where the outer peaks appear in the turbulence spectra [27]. This joint distribution between the positive and negative patterns is studied in terms of a binary sequence whose values are 1 when u'_{ref} and u' are simultaneously positive or negative. On the other hand, when the signs mismatch between u'_{ref} and u', the sequence attains zero. We refer to this as an overlap binary sequence and compute its lengths (N_p) by counting the consecutive occurrences where it stays at 1 or 0.

To quantify the information content in this binary sequence, Shannon entropies of the overlap event lengths (N_p) are considered and compared with a RS sequence by taking a ratio. Note that since synchronization is a relative measure, by only comparing the information content of the overlap event lengths with a RS sequence useful conclusions regarding synchronization can be drawn. This is because no synchronization or information exchange is expected between the two signals when they are randomly shuffled. Mathematically, Shannon entropy of the overlap event lengths with respect to a RS signal is computed as

$$H_n^{x_{\text{ref}},x}(N_p) = \frac{\sum_i P\left(N_{p,i}^{\text{RS}}\right) \ln\left[P\left(N_{p,i}^{\text{RS}}\right)\right]}{\sum_i P(N_{p,i}) \ln[P(N_{p,i})]}, \tag{1}$$

where x_{ref} is the reference signal, x is the signal from the traveling probe, and the summation is carried over all the possible consecutive sequences of 1 or 0.

The quantity $H_n^{x_{\text{ref}},x}(N_p)$ is bounded within, $0 \leqslant H_n^{x_{\text{ref}},x}(N_p) \leqslant 1$. Precisely, when $H_n^{x_{\text{ref}},x}(N_p)$ is 1, no difference exists between the original and RS signals, and therefore there is no synchronization between the occurrences of positive and negative events in the two signals. On the other hand, when $H_n^{x_{\text{ref}},x}(N_p)$ approaches zero [or, equivalently, $H_n^{x_{\text{ref}},x}(N_p) \ll 1$], the level of synchronization is quite strong since the arrangements of the overlap event lengths differ considerably from a random configuration. In Sec. III B we show how by combining the insights from level-crossing and event-synchronization analyses one can study the phenomenological features of the coherent structures in wall-bounded flows.

C. Surrogate models

In the context of turbulence research, surrogate models are employed to ascertain whether the statistical metrics used to measure certain turbulence properties are in fact sensitive to the underlying structures in the flow field [56]. The most common form of surrogate model is random shuffling, where the signal's PDF is preserved (thus its statistical moments) but the temporal structure is destroyed [44].

On the other hand, rank-surrogate models are used to alter the signal's PDF while preserving its temporal structure [57,58]. For instance, let us consider for a non-Gaussian turbulent signal, one samples the values from an equivalent Gaussian distribution. Thereafter, the newly sampled values are used to construct the turbulent time series while maintaining the same rank structure as the original signal. By doing so, the order of the values in the temporal sequence is preserved and hence the nature of dependencies between the adjacent points. Note that, instead of sampling the values

from a Gaussian distribution, one could, in fact, use a distribution that is a mixture of the original and Gaussian distributions.

Last, a more advanced surrogate model is iteratively adjusted amplitude Fourier transform (IAAFT) model where the signal's PDF and its autocorrelation functions are exactly preserved but the nonlinear dependencies between the signal values are destroyed through Fourier phase randomization. A detailed discussion of this model is presented in the review article by Lancaster *et al.* [44]. Therefore, by comparing any suitable statistical measure computed for the original and IAAFT surrogate model, one can infer about the role of nonlinearity on turbulence organization. In Sec. III C we demonstrate how these three different surrogate models help to unravel the interactions associated with coherent structures in our turbulent flow setup.

III. RESULTS AND DISCUSSION

We begin with describing how the information content of a turbulent signal changes when α is systematically varied. This aspect is utilized further to determine a set of critical α values, which we show to be related to the phenomenology of the coherent structures. By employing surrogate data, we identify that the statistical properties of u' at these critical α values can potentially serve as a metric to quantify inner-outer interaction in wall-bounded flows. We end our discussion with exploring a mechanism by which the large-scale coherent structures modulate the near-wall turbulent dynamics.

A. Level crossings and extreme values

To answer our first research question (see Sec. I), the probability distributions of event lengths $[P(N_p|_\alpha)]$ are investigated as α is varied. We consider $N_p|_\alpha$ since it is a discrete variable and represented through probability mass functions whose computation is insensitive to binning. Note that $N_p|_\alpha$ and $t_p|_\alpha$ are interchangeable through the relation, $t_p|_\alpha = N_p|_\alpha / f_s$. To characterize the stochastic variability and information content in $N_p|_\alpha$, we consider its Shannon entropy compared with a RS sequence of u'. The entropy is denoted as $H_n^{u'}(N_p|_\alpha)$, whose mathematical expression is provided in Eq. (A1) of Appendix A. Furthermore, $H_n^{u'}(N_p|_\alpha)$ is bounded between $0 \leqslant H_n^{u'}(N_p|_\alpha) \leqslant 1$ with 1 indicating a random configuration. From Fig. 2(a), one observes that the effect of changing α either from positive or negative side on $H_n^{u'}(N_p|_\alpha)$ is asymmetric. The vertical profiles of $H_n^{u'}(N_p|_{\alpha \geqslant 0})$ show an inflection point around $y^+ \approx 70$, while when α is approached from the negative side an another inflection point appears at $y^+ \approx 12$. The position $y^+ = 70$ indicates the location where the outer layer begins [59]. A recent study by Wang *et al.* [60] used $y^+ = 100$ instead of 70 to identify where the outer layer begins, but within the experimental errors we consider both these values to be nearly identical. On the other hand, at $y^+ = 12$, the inner-layer structures are active [27].

As shown later in Sec. III C, the asymmetrical progression in $H_n^{u'}(N_p|_\alpha)$, depending on whether α is greater or lesser than zero, is related to inner-outer interaction and nonlinearities in wall turbulence. However, these inflection points disappear with increasing α. In fact, $H_n^{u'}(N_p|_\alpha)$ tend towards unity at large α values [Fig. 2(b)]. This apparent randomness in N_p is associated with the fact that with increasing α, $t_p|_\alpha$ become statistically comparable to the integral scales (γ_u). This can be confirmed from Fig. 2(c), where the mean values of $t_p|_\alpha$ ($\overline{t_p|_\alpha}$) can be seen to exceed γ_u considerably as α increases. Since γ_u is the characteristic scale of the coherent structures [2–4], one can consider those α values as the critical ones (α_{th}) where the information content of N_p exactly matches with a RS signal. This condition implies $H_n^{u'}(N_p|_{\alpha_{\text{th}}}) = 1$. But for accuracy purposes, we compute these critical values when $H_n^{u'}(N_p|_\alpha)$ crosses 0.8 either from the positive or negative side (see Appendix A). These α values for the positive and negative sides are denoted as α_{th}^P and α_{th}^N [Fig. 2(b)], respectively, and any difference between them is correlated to the skewness of u' [$\mathcal{S}(u')$; Fig. 6(b)].

On considering $P(u')$, one can see the samples that exceed these critical values reside in the PDF tails [Fig. 2(d)]. For visualization purposes, before plotting $P(u')$, we scale the positive and

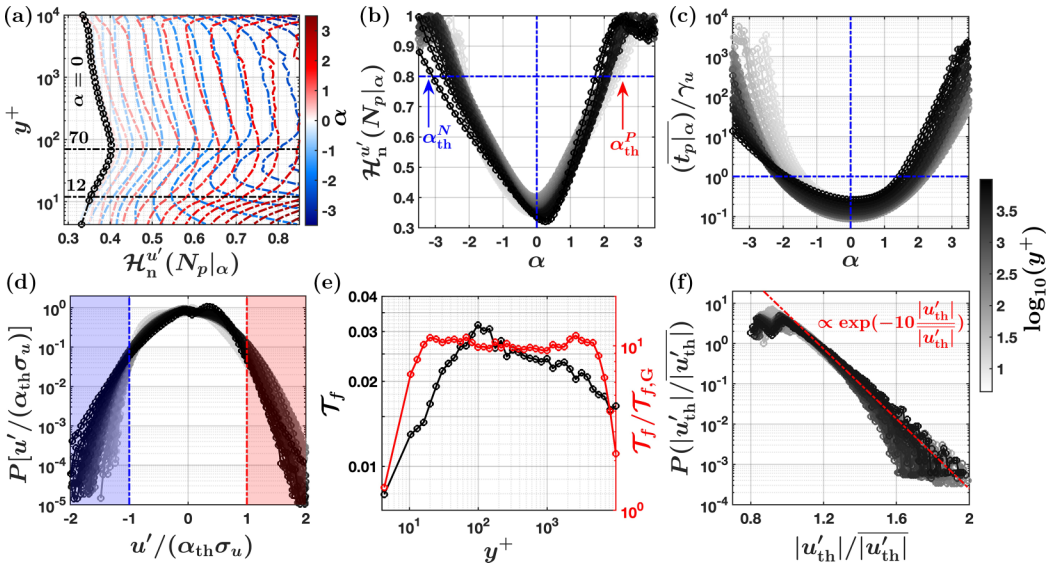

FIG. 2. From the T1 dataset, (a) vertical profiles of Shannon entropies $[\mathcal{H}_n^{u'}(N_p|_\alpha)]$, corresponding to the event lengths at different α levels ($N_p|_\alpha$) are shown; (b) $\mathcal{H}_n^{u'}(N_p|_\alpha)$ values are plotted for different y^+ values (see the color bar), and α_{th}^N and α_{th}^P are identified where $\mathcal{H}_n^{u'}(N_p|_\alpha) = 0.8$; and (c) normalized mean timescales ($\overline{t_p|_\alpha}/\gamma_u$) are plotted against α values, where the horizontal blue dash-dotted line indicates $\overline{t_p|_\alpha} = \gamma_u$. (d) The PDFs of $u'/(\alpha_{th}\sigma_u)$ are shown, where shaded regions indicate the critical u' samples satisfying either $u' \geqslant \alpha_{th}^P\sigma_u$ (red-shaded region) or $u' \leqslant \alpha_{th}^N\sigma_u$ (blue-shaded region); (e) time fractions ($\mathcal{T}_f$) occupied by the critical u' samples (u'_{th}) and their comparison with a Gaussian distribution ($\mathcal{T}_{f,G}$) are shown; and (f) PDFs of $|u'_{th}|/\overline{|u'_{th}|}$ are shown, where the absolute values of u'_{th} are undertaken.

negative u' values with $\alpha_{th}^P\sigma_u$ and $\alpha_{th}^N\sigma_u$, respectively. Under this scaling, the values beyond ± 1 in Fig. 2(d), indicate those critical u' samples (u'_{th}) exceeding either $\alpha_{th}^P\sigma_u$ (red-shaded regions) or $\alpha_{th}^N\sigma_u$ (blue-shaded regions). Specifically, from Fig. 2(e), the time fractions ($\mathcal{T}_f$) associated with these critical samples (u'_{th}) are nearly 1–3% of the total sample length (i.e., in the 97 to 99 percentile range), and their values differ significantly from the ones obtained through a Gaussian distribution of u' ($\mathcal{T}_{f,G}$). Mathematically, $\mathcal{T}_{f,G}$ is computed by integrating the Gaussian distribution between the limits $-\infty$ and $\alpha_{th}^N\sigma_u$ or $\alpha_{th}^P\sigma_u$ and $+\infty$. The non-Gaussian tails in u' are thus quantified through the ratio $\mathcal{T}_f/\mathcal{T}_{f,G}$, and since $\mathcal{T}_f \gg \mathcal{T}_{f,G}$, their values remain substantially larger than unity as evident from Fig. 2(e). Accordingly, $P(|u'_{th}|/\overline{|u'_{th}|})$ follow an exponential distribution [Fig. 2(f)], compliant with the theory of extreme value statistics [61,62]. Note that we consider the absolute values of u'_{th} and scale them further with $\overline{|u'_{th}|}$. This is because the PDFs of u'_{th} remain nearly the same irrespective of the sign and the scaling with the mean of the absolute values produces the best collapse.

B. Identifying coherent structures

Next, we establish that u'_{th} carry the signatures of the outer-layer coherent structures. This is achieved through a two-step process, first by applying event-synchronization analysis and later classifying the positive and negative u' events into two distinct categories. Below, we discuss these steps one by one.

1. Event synchronization

In wall turbulence, the presence of hairpin structures organize the streamwise velocity field into alternating high- ($u' > 0$) and low-speed ($u' < 0$) streaks [10]. This, in turn, induces positive and

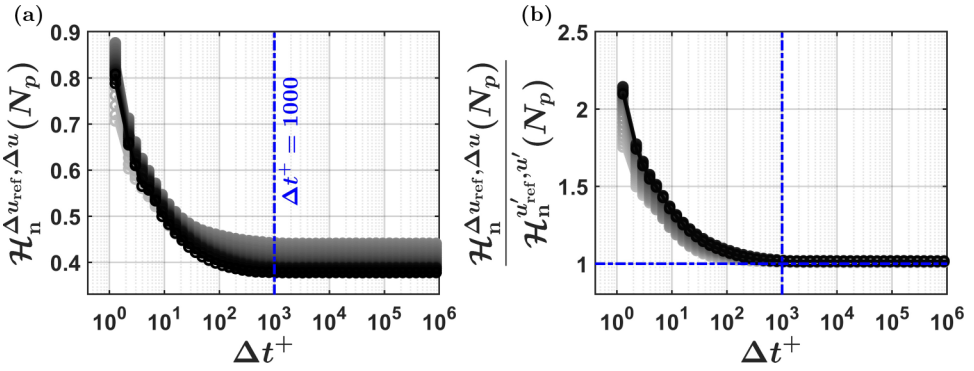

FIG. 3. For the T1 dataset, (a) Shannon entropies of the synchronized event lengths [see Eq. (1)] are plotted against different time lags (Δt^+), where Δu denotes the velocity increments, and (b) the same Shannon entropies are shown but their values are scaled by the entropies of the synchronized event lengths computed for the full signal.

negative fluctuations in u' signals. Through an event synchronization analysis (see Sec. II B), we identify how well these positive and negative patterns are coupled with each other across y^+. To incorporate the effect of turbulent scales, the analysis is carried on the Δu_{ref} and Δu signals, where Δu denotes velocity increments $[u'(t+\Delta t) - u'(t)]$ at a time lag Δt. Specifically, Δu_{ref} indicates the increments computed from the u'_{ref} signals at $y^+ = 4.3$, while Δu represents the ones computed from the u' signals at any height other than $y^+ = 4.3$. The time lags are normalized with wall scaling and denoted as Δt^+ ($\Delta t \times u_*^2/\nu$). Note that $H_n^{\Delta u_{\text{ref}},\Delta u}(N_p)$ is bounded between 0 to 1, where 1 (0) indicates no (complete) synchronization.

From Fig. 3(a), one observes that the positive and negative events across all y^+ values are most strongly coupled at scales $\Delta t^+ \geqslant 1000$ (Δt^+ is the normalized time lag). In fact, if the synchronized entropy values at any Δt^+ are scaled with the entropy values for the full signal, then $[H_n^{u'_{\text{ref}},u'}(N_p)]$, then $H_n^{\Delta u_{\text{ref}},\Delta u}(N_p)$ approaches $H_n^{u'_{\text{ref}},u'}(N_p)$ at scales $\Delta t^+ \geqslant 10^3$ [Fig. 3(b)]. The scale $\Delta t^+ = 10^3$ is commensurate with the outer spectral peak as estimated from the premultiplied u' spectra presented in Baars *et al.* [27] and Iacobello *et al.* [52] and therefore physically represents the timescales of the outer-layer structures. This implies at scales comparable to outer-layer structures the synchronized entropies of the velocity differences become equal to the full signal values. Thus, one could infer that the positive and negative patterns in the u' signals (i.e., $u' > 0$ and $u' < 0$ events), occurring at heights deep within the inner layer, preserve information about the outer-layer structures.

2. *Conditional event sampling*

To extract that information, we conditionally select the events based on whether they contain the samples satisfying $u' \geqslant \alpha_{\text{th}}^P \sigma_u$ and $u' \leqslant \alpha_{\text{th}}^N \sigma_u$ (l-type events) or not (s-type events). The acronyms l and s represent large and small, respectively, whose justification will become clear as we discuss the results. The concepts of l- and s-type events are graphically illustrated in Fig. 4(a), where we use a segment of the u' time series at $y^+ = 66.84$ for explanatory purposes. In Fig. 4(a), the three dash-dotted horizontal lines indicate $\alpha = 0$ (black), α_{th}^P (red), and α_{th}^N (blue) levels. The l-type events are defined as those positive or negative blocks where at least one of the u' samples satisfy the relation $u' \geqslant \alpha_{\text{th}}^P \sigma_u$ and $u' \leqslant \alpha_{\text{th}}^N \sigma_u$. On the other hand, s-type events are those which do not satisfy the above condition. To distinguish the l-type events from s-type ones, we use red-(blue) shaded regions to indicate the l-(s)type events. The timescales associated with l-and s-type events are denoted as $t_p|_l$ and $t_p|_s$ respectively, as shown in Fig. 4(a). These timescales are subsequently normalized with γ_u, which is the integral scale of the u' signal.

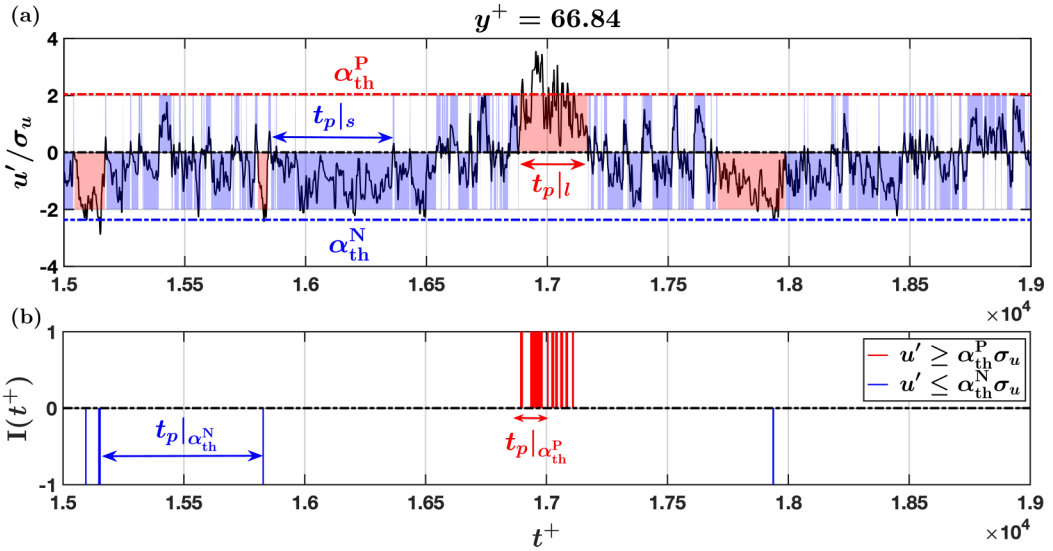

FIG. 4. (a) The concept of l- and s-type events are illustrated through a segment of a u' time series at $y^+ = 66.84$ from the T1 dataset. Note that u' is normalized by its standard deviation σ_u and the time axis (t^+) is scaled by the wall units. The thresholds α^P_{th} and α^N_{th}, identified from the Shannon entropy curves [see Fig. 2(b)], are shown as horizontal red and blue dash-dotted lines, respectively. The red-colored events (l-type events) contain at least one of these thresholds, whereas the blue-colored ones (s-type events) do not contain any of these. The timescales associated with l- and s-type events are denoted as $t_p|_l$ and $t_p|_s$, respectively. (b) The temporal locations of the samples satisfying $u' \geqslant \alpha^P_{\mathrm{th}}\sigma_u$ and $u' \leqslant \alpha^N_{\mathrm{th}}\sigma_u$ are shown for the same segment of the time series. For identification purposes, an identity function $\mathrm{I}(t^+)$ is used that takes a value of $+1$ when the samples exceed $u' \geqslant \alpha^P_{\mathrm{th}}\sigma_u$ (red bars), -1 when the samples satisfy $u' \leqslant \alpha^N_{\mathrm{th}}\sigma_u$ (blue bars), and zero otherwise. The timescales associated with the positive and negative samples are denoted as $t_p|_{\alpha^P_{\mathrm{th}}}$ and $t_p|_{\alpha^N_{\mathrm{th}}}$, respectively.

In the lower panel of Fig. 4 [i.e., Fig. 4(b)], we also show where the samples exceeding $u' \geqslant \alpha^P_{\mathrm{th}}\sigma_u$ and $u' \leqslant \alpha^N_{\mathrm{th}}\sigma_u$ are temporally located. For this purpose, we use an identity function $\mathrm{I}(t^+)$ that takes a value of $+1$ when the samples exceed $u' \geqslant \alpha^P_{\mathrm{th}}\sigma_u$ (red bars), -1 when the samples are below $u' \leqslant \alpha^N_{\mathrm{th}}\sigma_u$ (blue bars), and zero otherwise. It is evident from Fig. 4(b) that the negative samples are wide apart in time, while the positive samples appear to be more closely connected. The timescales associated with the positive and negative samples are denoted as $t_p|_{\alpha^P_{\mathrm{th}}}$ and $t_p|_{\alpha^N_{\mathrm{th}}}$, respectively. More evidence on the asymmetry between $t_p|_{\alpha^P_{\mathrm{th}}}$ and $t_p|_{\alpha^N_{\mathrm{th}}}$ and its physical reason will be presented in Sec. III C.

The contributions from a particular event (either l- or s- type) to the velocity variance is defined as

$$\langle A_{uu}|t_p\rangle = \frac{1}{T}\int_t^{t+t_p} u'^2(t)\,dt, \tag{2}$$

where t_p could be either $t_p|_l$ or $t_p|_s$ and T is the total signal duration. Note that $\langle A_{uu}|t_p\rangle$ values are scaled with the friction velocity and further divided by the logarithmic bin width of t_p so the estimations remain nearly independent of the bin choice. For brevity, henceforth, we denote the wall-normalized quantity $\langle A^+_{uu}|t_p\rangle$ simply as $\langle A^+_{uu}\rangle$. Typically, the number of detected l-type events is of the order of 10^3, as compared to 10^5, for the s-type ones. In Appendix B, we provide an interesting analysis to explore the effects of α on the statistics of l- and s-type events.

In Figs. 5(a)–5(b), the contributions from l- or s-type events ($\langle A^+_{uu}\rangle$) against their timescales to streamwise velocity variance (σ_u^2) are plotted separately. Notably, most of the contributions from l-type events to σ_u^2 come from the heights in and around $y^+ = 474$, where the influence of the

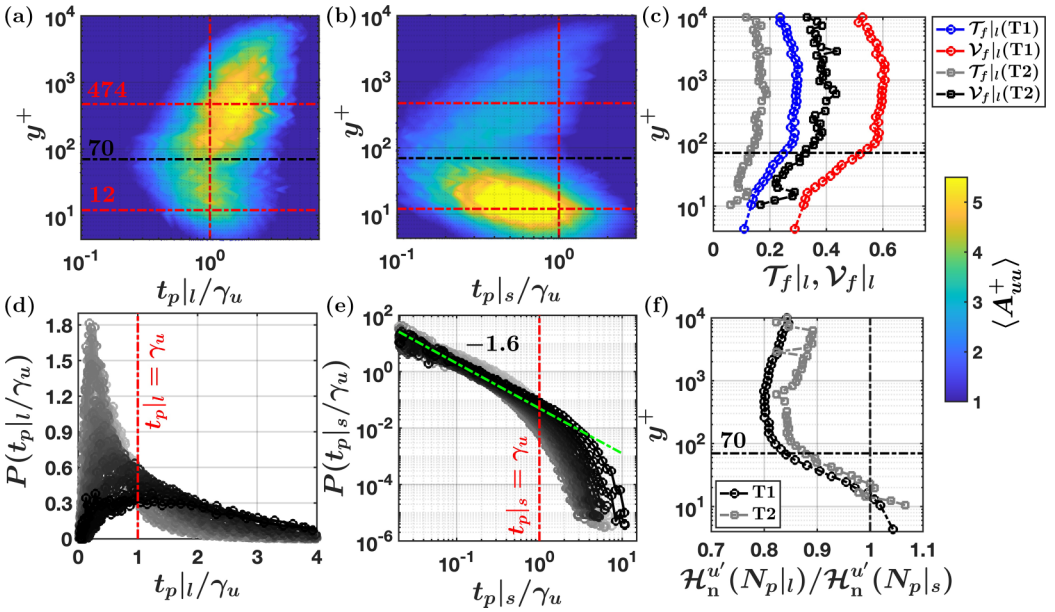

FIG. 5. The contours of event amplitudes $[\langle A^+_{uu} \rangle$, see Eq. (2)] are plotted separately for the (a) l- and (b) s-type events from T1 dataset. The timescales of these events are denoted as $t_p|_l/\gamma_u$ and $t_p|_s/\gamma_u$, where γ_u is the integral timescale. The two red dash-dotted horizontal lines indicate the positions $y^+ = 474$ and 12, respectively. The horizontal black dash-dotted line denotes $y^+ = 70$, while the vertical red lines indicate $t_p/\gamma_u = 1$. (c) Fractional contributions of l-type events to the variance $(\mathcal{V}_f|_l)$ and occupation time $(\mathcal{T}_f|_l)$ are shown. The PDFs of (d) $t_p|_l/\gamma_u$ and (e) $t_p|_s/\gamma_u$ are shown from T1 dataset. (f) Shannon entropy ratios of N_p corresponding to l- and s-type events are plotted.

outer-layer structures are the strongest [27]. From Fig. 5(a), it is even conspicuous that the timescales involved with the maximum contributions exceed at least twice the integral scales. In turbulent boundary layers, $\gamma_u \overline{u} \approx 0.5\delta$ [3], where δ is the boundary layer height. Therefore, the scales of the active l-type events are comparable to δ, which physically represents the large- and very large scale motions. Regarding s-type events, they contribute the most at heights $y^+ = 12$ where the inner-layer structures reside [27], with the timescales being considerably smaller than γ_u. Thus, in simple words, the l-type events remain most active in the outer layer, while the s-type ones dominate the inner-layer dynamics. Quite possibly, the s-type events represent the near-wall bursting phenomenon [31].

To evaluate the total fractional contributions from any event types to the velocity variance $(\mathcal{V}_f)$, one could simply add up all the $\langle A_{uu}|t_p \rangle$ values and divide by σ_u^2. On the other hand, for the occupation time fractions $(\mathcal{T}_f)$, all the $t_p|_l$ or $t_p|_s$ values are summed up and divided by the signal duration T. These fractions satisfy the additive property, such as $x_f|_l + x_f|_s = 1$, where x is either $\mathcal{V}$ or $\mathcal{T}$, and the subscripts denote the s- and l-type events. At heights $y^+ > 70$, the total contributions from l-type events to the velocity variance $(\mathcal{V}_f|_l)$ remain between 40 and 60%, despite occupying only ≈20–30% of the time $[\mathcal{T}_f|_l$, see Fig. 5(c)]. Although some variations in $\mathcal{V}_f|_l$ and $\mathcal{T}_f|_l$ are noted between T1 and T2 datasets, they disappear if one considers an intermittency ratio, $(\mathcal{V}_f|_l)/(\mathcal{T}_f|_l)$, whose values are close to 2. Most importantly, the contributions from l-type events towards σ_u^2 compare well with those from LSMs and VLSMs in wall turbulence [22], corroborating our previous observation [Fig. 5(a)].

Moreover, the PDFs of $t_p|_l/\gamma_u$ and $t_p|_s/\gamma_u$ appear to be quite different [Figs. 5(d)–5(e)]. Specifically, $P(t_p|_l/\gamma_u)$ follows a log-normal distribution (verified with q-q plots), while $P(t_p|_s/\gamma_u)$ is a power law of exponent -1.6 with an exponential cut off at scales comparable to γ_u. It is interesting to note that $P(t_p|_s/\gamma_u)$ agrees reasonably well with the traditional zero-crossing PDFs of $t_p|_{\alpha=0}$, as

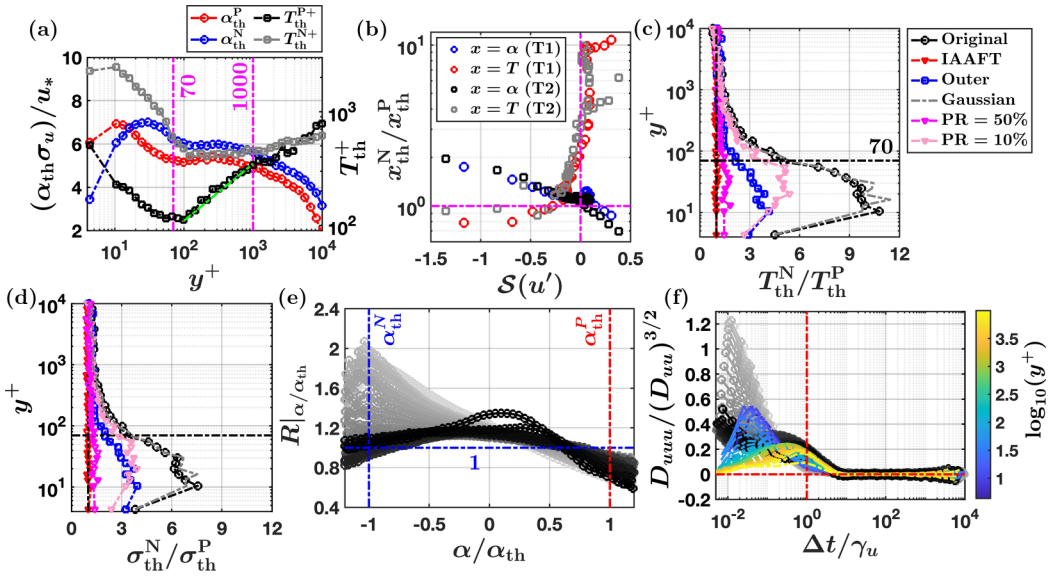

FIG. 6. (a) Wall-normalized velocity ($\alpha_{\mathrm{th}}\sigma_u/u_*$) and mean timescales ($T^+_{\mathrm{th}}$), evaluated at the α_{th} levels, are shown for the T1 dataset. The green dash-dotted line indicates the growth of T^{P+}_{th} with height as $(y^+)^{1/2}$. (b) Scatter plots between $x^N_{\mathrm{th}}/x^P_{\mathrm{th}}$ ($x = \alpha, T$) and $\mathcal{S}(u')$ are plotted. For the T1 dataset, ratios of (c) mean timescales ($T^N_{\mathrm{th}}/T^P_{\mathrm{th}}$) and (d) their standard deviations ($\sigma^N_{\mathrm{th}}/\sigma^P_{\mathrm{th}}$) are compared with Gaussian rank surrogate, phase-randomized surrogate, and with a Fourier-filtered signal for which the outer-layer influences are removed; (e) the mean level-crossing timescales at different $\alpha/\alpha_{\mathrm{th}}$ levels are compared with a phase-randomized signal, where $R|_{\alpha/\alpha_{\mathrm{th}}}$ denotes the ratios between the two; and (f) third-order structure function skewness $[D_{uuu}/(D_{uu})^{3/2}]$ are compared between the original (gray shaded lines) and a conditionally shuffled signal (colored lines).

shown in Fig. S1b of [53]. This indicates, the log-normal distribution of $P(t_p|_l/\gamma_u)$ is only possible to obtain when the events are separated into these two categories. In the context of turbulence literature, log-normal distributions are usually employed to describe the statistics of turbulence dissipation [54,63], while we associate it with the l-type event sizes.

In general, log-normal distributions are associated with multiplicative growth processes [64,65], and the fact that LSMs and VLSMs are formed by accumulating hairpin eddies [10,66] provides a compelling argument regarding why we observe such distributions for l-type events. This reasoning seems even more plausible when one observes that, as opposed to s-type events, $P(t_p|_l/\gamma_u)$ display a clear dependence on height, with its peaks (modes) being shifted to larger $t_p|_l/\gamma_u$ values as y^+ increases. Furthermore, by considering the Shannon entropies of event lengths, l-type events are more organized than the s-type ones [since $H_n^{u'}(N_p|_l) \ll H_n^{u'}(N_p|_s)$] as y^+ approaches the outer layer [Fig. 5(f)]. These outcomes confirm that the detected extremes in u' (u'_{th}) carry the signatures of the outer-layer structures and are further utilized to infer about the velocity scales and inner-outer interaction in wall turbulence. Although in Figs. 5(a) and 5(b) and Figs. 5(d) and 5(e), T1 dataset is considered, similar findings are obtained for T2 dataset also (see Fig. S2 in Ref. [53]).

C. Connections to the turbulent dynamics

We construct a velocity scale ($\alpha_{\mathrm{th}}\sigma_u$) for the outer-layer structures and plot their profiles against y^+ in Fig. 6(a). For $70 < y^+ < 10^3$ (i.e., the log layer), this scale attains a near-constant value of $\approx 5u_*$. This is consistent with the observation that the vertical profiles of α^P_{th} and α^N_{th} are invariant in the log layer, such that $\alpha^P_{\mathrm{th}} \approx 2$ and $\alpha^N_{\mathrm{th}} \approx 2.2$ (not shown). It remains interesting to see whether

this velocity scale, as obtained from the critical α values, can better collapse the turbulence statistics among different experiments. This exercise is out of scope of the present study.

On the other hand, to assess the influence of outer-layer structures on turbulence organization from u' time series, we consider the mean timescales at $\alpha = \alpha_{\text{th}}$ level ($T_{\text{th}} = \overline{t_p|_{\alpha_{\text{th}}}}$). In practice, T_{th} represents the mean spacing between u'_{th} values, which are the peaks and troughs of the u' signal depending on the sign. The wall-normalized mean timescales for the positive and negative side are denoted as T_{th}^{P+} and T_{th}^{N+}, respectively, with their behaviors being very different [Fig. 6(a)]. For instance, in the inner layer ($y^+ < 70$), the timescales T_{th}^{N+} exceed T_{th}^{P+} considerably with both showing a decreasing trend as y^+ increases. In terms of integral scales, T_{th}^{N} values can exceed γ_u by as much as 20 times at heights $y^+ < 70$ [Fig. 9(d) in Appendix C]. However, in the log layer ($70 < y^+ < 10^3$), T_{th}^{P+} increases as $(y^+)^{1/2}$ [see the green dash-dotted line in Fig. 6(a)], while T_{th}^{N+} is nearly constant at 10^3. This increase of T_{th}^{P+} in the log layer can be explained by considering how the hairpin structures merge progressively to form LSMs and VLSMs [10], whose characteristic scales ($\approx 10^3$ wall units [67]) match with T_{th}^{N+} values. Beyond the outer layer, T_{th}^{P+} and T_{th}^{N+} values almost overlap with each other. This gives a firsthand indication that the inequality between T_{th}^{P} and T_{th}^{N} could possibly be connected to how the energetic structures interact in wall turbulence. We expand on this point below.

Unlike $\alpha_{\text{th}}^{N}/\alpha_{\text{th}}^{P}$, the difference between T_{th}^{P} and T_{th}^{N} (quantified through their ratio, $T_{\text{th}}^{N}/T_{\text{th}}^{P}$) is anticorrelated to $\mathcal{S}(u')$ [Fig. 6(b)]. Particularly, for both datasets, the largest values of $T_{\text{th}}^{N}/T_{\text{th}}^{P}$ are obtained when the skewness of u' is nearly zero [Fig. 6(b)]. From Fig. 6(c), one could also notice that $T_{\text{th}}^{N}/T_{\text{th}}^{P}$ values reach a maximum at $y^+ = 12$ and continue to remain larger than 1 up to heights $y^+ \approx 10^3$, beyond which they return to unity. At this point, one may wonder what properties of a time series cause the nonunity values of $T_{\text{th}}^{N}/T_{\text{th}}^{P}$. To scrutinize this aspect more carefully, we employ surrogate data analysis by generating a Fourier phase-randomized (PR) u' signal that preserves the Fourier amplitudes but randomizes its phases, thereby keeping the same Fourier spectrum or the autocorrelation function as the original signal. We use an IAAFT model for PR purposes, which, in addition to the autocorrelation function, also preserves the signal PDFs [44]. Clearly, from Fig. 6(c), $T_{\text{th}}^{N}/T_{\text{th}}^{P}$ approaches 1 for a PR time series, thereby nullifying any asymmetry between them (see red dash-dotted line). This implies, the nonunity values of $T_{\text{th}}^{N}/T_{\text{th}}^{P}$ are uniquely determined by an underlying order in the Fourier phases, and therefore, are sensitive to how the coherent structures are organized. This conclusion is supported by the fact that the ordering in Fourier phases is associated with the organizational aspects of coherent structures in a turbulent flow [68–70]. We carry out some additional tests to confirm this connection.

To demonstrate how sensitive $T_{\text{th}}^{N}/T_{\text{th}}^{P}$ is to the Fourier phases, if instead of 100%, only 10–50% of the Fourier phases are randomized that itself has a significant effect on $T_{\text{th}}^{N}/T_{\text{th}}^{P}$ (shown as dash-dotted lines with lighter red shades). Contrarily, if $P(u')$ are transformed to Gaussian while maintaining the temporal structure (otherwise known as Gaussian rank surrogate [57]), then $T_{\text{th}}^{N}/T_{\text{th}}^{P}$ overlaps with the original [gray dash-dotted line indicates the Gaussian rank surrogate in Fig. 6(c)]. Specifically, if certain rank surrogates are generated whose PDFs are a mixture of Gaussian and original ones with an identical temporal structure, then no effects on $T_{\text{th}}^{N}/T_{\text{th}}^{P}$ are observed when the mixture ratios are altered (not shown). Hence, not the PDFs (containing all the statistical moments of u') but the temporal organization of the u' signal sets the values of $T_{\text{th}}^{N}/T_{\text{th}}^{P}$.

Physically, the passage of coherent structures over a measurement location dictates how the u' values are temporally arranged, and therefore, should encode information about the outer-layer structures. Given this premise, if one removes the outer-layer influences by choosing a Fourier cut-off filter at $\lambda^+ = 7000$ (where λ is the streamwise wavelength) and apply inverse Fourier transform [27], then it changes $T_{\text{th}}^{N}/T_{\text{th}}^{P}$ considerably [see blue dash-dotted line in Fig. 6(c)]. In fact, if the wavelengths corresponding to the inner-layer structures are also removed by choosing $\lambda^+ = 1000$ [27], then it forces $T_{\text{th}}^{N}/T_{\text{th}}^{P}$ to be nearly 1 across all y^+ values. By repeating the analysis on the ratios of the standard deviations or any other higher-order statistics (for instance, skewness and kurtosis) of $t_p|_{\alpha_{\text{th}}}$, the outcome remains the same. However, for illustration purposes, we only show the results

in Fig. 6(d) corresponding to the standard deviations of $t_p|_{\alpha_{\rm th}}$ ($\sigma^N_{\rm th}/\sigma^P_{\rm th}$). Thus, one can conclude that the statistical asymmetry between $t_p|_{\alpha^P_{\rm th}}$ and $t_p|_{\alpha^N_{\rm th}}$ signifies the impact of outer-layer structures on turbulence organization and could be used as a metric to quantify inner-outer interaction in wall turbulence, as an alternative to the amplitude modulation coefficient proposed by Mathis *et al.* [23].

Notwithstanding the fact that a large body of literature exists on quantifying the inner-outer interaction in wall turbulence through amplitude modulation coefficient [26], they are all based on spectral domain (either Fourier or wavelets) where cut-off wavelengths are used to separate the contributions from large and small scales. By contrast, our metric (for simplicity purposes we use only the first-order moment $T^N_{\rm th}/T^P_{\rm th}$) quantifies this interaction strictly based on the temporal domain, where the inner- and outer-scale motions are separated by choosing appropriate thresholds from the Shannon entropy curves [Fig. 2(b) and Figs. 5(a) and 5(b)]. Also, as demonstrated before, the nonunity values of $T^N_{\rm th}/T^P_{\rm th}$ are not related to the signal's PDF or skewness, and therefore, do not suffer from a drawback associated with amplitude modulation coefficient as outlined in Schlatter and Örlü [71]. Nevertheless, in spite of their different conceptual origins, the variations in $T^N_{\rm th}/T^P_{\rm th}$ with y^+ are qualitatively similar to the amplitude modulation coefficient, such that for both metrics, the largest values are obtained within the inner layer. We next establish that the asymmetry between $T^N_{\rm th}$ and $T^P_{\rm th}$ captures an important physics of wall-bounded flows, not immediately obvious from spectral analysis.

To do so, we consider the point that a PR procedure destroys nonlinear dependencies in a signal [44], thereby indicating that the nonunity values of $T^N_{\rm th}/T^P_{\rm th}$ are related to nonlinear dynamics. This is at odds with persistence or zero-crossing analysis, where the timescale statistics depend only on the autocorrelation functions (or the Fourier spectrum) accounting for the signal's linear structure [38,72]. As one's intuition might suggest, by increasing α, the statistics of $t_p|_\alpha$ rely less and less on the linear correlations [see Fig. 1(c)] but become more sensitive to the nonlinear dependencies in a time series. Therefore, the level-crossing statistics could unveil hidden nonlinearities in a stochastic signal and provide more information about coherent structures than from spectral analysis alone. To establish this feature more convincingly, in Fig. 6(e), we show how the mean timescales ($\overline{t_p|_\alpha}$) change between the original and PR signal, as α is varied systematically. This is quantified through a timescale ratio defined as

$$R|_{\alpha/\alpha_{\rm th}} = \frac{\overline{t_p|_{(\alpha/\alpha_{\rm th})}}}{[\overline{t_p|_{(\alpha/\alpha_{\rm th})}}]_{\rm PR}}, \tag{3}$$

where $\alpha_{\rm th}$ could be either $\alpha^P_{\rm th}$ or $\alpha^N_{\rm th}$, depending on whether α is approached from the positive or negative side. As the ratio $R|_{\alpha/\alpha_{\rm th}}$ deviates from unity, strong nonlinear dependencies regulate the timescale statistics.

Apparently, for heights within the inner layer, nonlinear dependencies have the strongest effects on $\overline{t_p|_\alpha}$ at $\alpha_{\rm th}$ level [Fig. 6(e)]. More importantly, this nonlinearity influences $\overline{t_p|_\alpha}$ the most when the threshold is approached from the negative side ($\alpha^N_{\rm th}$). The $\alpha^N_{\rm th}$ ($\alpha^P_{\rm th}$) values represent the fluctuations $u' < 0$ ($u' > 0$), and since these thresholds carry the signatures of the outer layer structures [see Figs. 5(a) and 5(b)], they physically represent the large-scale low (high) speed streaks. Therefore, as our results suggest, compared to the outer-layer high-speed streaks, the low-speed ones interact more nonlinearly with the near-wall turbulent motions. The role of nonlinearity can be reconciled with previous results where it is established that the scale interactions in turbulent flows are essentially a nonlinear phenomenon caused by the presence of inertial terms in the governing Navier-Stokes equations [23,24,73]. However, it is not immediately clear why the effect of this nonlinearity is felt more strongly when the thresholds are varied from the negative side.

Previous research has shown that at locations very close to the wall, the outer-layer motions have different effects on the near-wall turbulent dynamics depending on its sign [23,74]. For instance, for a zero-pressure-gradient turbulent boundary layer flow, Mathis *et al.* [23] found that the near-wall turbulent motions were energized when the large-scale streamwise velocity fluctuations were positive while they appeared to be suppressed when the same were negative. Similar evidence was

put forth by Guala *et al.* [75] using observations from a high-Reynolds-number atmospheric flow. It is thus interesting to ask whether such asymmetrical effects of outer-layer motions on the near-wall turbulent dynamics are indeed related to the nonlinear terms in the Navier-Stokes equations? This is out of the scope of present work and further research is needed to understand this aspect. Nevertheless, such nonlinear effects on $\overline{t_{p|\alpha}}$ become irrelevant when the absolute values of u' are considered (see Appendix C). This outcome confirms that the events detected from the absolute signals do not obey the turbulent flow physics.

In turbulent flows, the energy is injected at the scales of coherent structures and subsequently cascades down to smaller and smaller scales, eventually reaching the dissipation scale. To further investigate the influence of these outer-layer structures on the energy cascading process, we consider a u' time series where only the values exceeding $\alpha^P_{\text{th}}\sigma_u$ and $\alpha^N_{\text{th}}\sigma_u$ (i.e., the u'_{th} samples) are randomly shuffled while the others are kept intact. This operation selectively destroys the turbulence organization associated with outer-layer structures. We subsequently calculate the third-order structure function skewness $[D_{uuu}/(D_{uu})^{3/2}$, where $D_{uuu} = \overline{(\Delta u)^3}$ and $D_{uu} = \overline{(\Delta u)^2}]$, as its nonzero values are related to the turbulence kinetic energy cascading from large to small scales [76]. These skewness values are negative when the spatial lags (r) are considered, but they remain positive in the temporal domain since $r = -\overline{u} \times \Delta t$ (Taylor's hypothesis). If $D_{uuu}/(D_{uu})^{3/2}$ are compared between the original and conditionally shuffled signal, at scales smaller than γ_u, then $D_{uuu}/(D_{uu})^{3/2}$ of the conditionally shuffled signals decreases significantly with increasing y^+ [Fig. 6(f)]. Since within the inner layer the kinetic energy is also carried by the inner-layer structures, $D_{uuu}/(D_{uu})^{3/2}$ values remain slightly larger for the conditionally shuffled signal. Apart from $D_{uuu}/(D_{uu})^{3/2}$ approaching zero, this conditional-shuffling procedure destroys the inertial subrange scaling in second-order structure functions (Fig. S3 in Ref. [53]). Therefore, we establish the impact of outer-layer coherent structures on the energy cascade in wall turbulence. It is important to note that these outcomes from Fig. 6 remain unchanged whether T1 or T2 datasets are considered (Fig. S4 in Ref. [53]).

IV. CONCLUSION

In this study, we introduce a data-driven coherent structure detection scheme and implement the same on two well-established wall turbulence time-series datasets. This scheme is based on the level-crossing properties of a stochastic time series, and the structures being identified from this scheme comply with the phenomenology of the coherent structures in wall-bounded flows. In particular, this detection scheme does not require any external inputs or arbitrary thresholds, thereby making it an attractive choice in experimental turbulence research. This flexibility is advantageous for atmospheric flows, since most of the field experiments conducted in an atmospheric boundary layer measure the turbulent variables at only a few specific heights on a tower. Therefore, it is difficult to ascertain the presence of coherent structures from these measurements alone, but by conducting a level-crossing analysis it might be possible to get some insights about these structures. In recent times, the deployment of particle velocimetry setups to study atmospheric turbulence is becoming increasingly common [77] and thus the findings from level-crossing analysis can be complemented with the spatial information available from these data.

Moreover, through level-crossing approach, we provide comprehensive evidence that the inner-outer interaction in wall turbulence can be linked to a statistical asymmetry between the peaks and troughs of streamwise velocity fluctuations. For simplicity, this asymmetry is quantified by taking a ratio between the mean timescales associated with the peaks and troughs of the u' signal. These extremes are identified from the Shannon entropy curves of event lengths plotted against various threshold levels. Additionally, by employing phase-randomized surrogate data, we demonstrate that the level-crossing statistics are quite sensitive to the nonlinear dependencies in the u' signal. In physical terms, this finding implies that the outer-layer coherent structures (LSMs and VLSMs) modulate the near-wall turbulent dynamics through a nonlinear interaction associated with low-speed streaks, a mechanism not identifiable from spectral analysis alone.

For future research endeavors, it would be interesting to compare the peak-trough asymmetry parameter among different experiments in wall-bounded turbulence, spanning both internal and external flows, a wide range of Reynolds numbers, and different surface conditions (i.e., rough vs. smooth). Since this asymmetry parameter is sensitive to how the outer-layer coherent structures nonlinearly interact with the near-wall dynamics, such comparisons would shed more light on the physics of wall-bounded turbulence. Although through level-crossing framework we successfully extract the signatures of inner- and outer-layer structures from time-series measurements, due to the lack of spatial information it is difficult to ascertain their topological features, and therefore, remains as a future work. Nevertheless, it is prudent to extend the level-crossing approach to momentum flux time series. By studying the Shannon entropy curves of flux events, it is possible to determine an appropriate size of a quadrant hole (instead of choosing those arbitrarily) for detecting intense activities. On the interdisciplinary front, the level-crossing framework can be used to detect extremes in other dynamical systems (hydrology, stock markets, etc.), or to generate training datasets for state-of-the-art machine learning models, which often fail to predict the extreme occurrences.

ACKNOWLEDGMENTS

S.C. and T.B. acknowledge the funding support from the US National Science Foundation (Grants No. NSF-AGS-PDM-2146520, No. NSF-OISE-2114740, No. NSF-CPS-2209695, No. NSF-ECO-CBET-2318718, and No. NSF-DMS-2335847), the University of California Office of the President (UCOP-LFR-20-653572), NASA (80NSSC22K1911), and the United States Department of Agriculture (Grants No. NIFA 2021-67022-35908 and No. USDA-20-CR-11242306-072). The authors thank the anonymous reviewers for their comments that helped to improve the paper. SC thanks Giovanni Iacobello for some initial feedback on the first draft of this paper.

APPENDIX A: STATISTICAL ROBUSTNESS OF EVENT ENTROPY CURVES

We begin by plotting the scaled Shannon entropies of the event lengths (with respect to a RS signal) where α values are normalized with either $\alpha_{\rm th}^{P}$ or $\alpha_{\rm th}^{N}$ (depending on the sign), denoted together as $\alpha_{\rm th}$. Owing to how $\alpha_{\rm th}$ is defined, this normalization ensures that the scaled Shannon entropy curves collapse at 0.8 for all the y^+ values [Fig. 7(a)]. However, it raises a question of why we consider 0.8 as our choice instead of 1.

To explain the philosophy behind 0.8, first let us recall that in this study, we attempt to extract the features of time series that are representative of the coherent structures in the flow. To achieve that objective we exploit two facts: first, the characteristic scale of coherent structures is the integral scale, and second, since the time-series values are uncorrelated beyond the integral scales the PDFs of their interarrival times would be analogous to a RS signal. Therefore, in an ideal scenario, one would have considered $\alpha_{\rm th}$ when $\mathcal{H}_n^{u'}(N_p|_\alpha)$ was exactly 1. However, our choice of 0.8 is influenced by the statistical accuracy associated with $\mathcal{H}_n^{u'}(N_p|_\alpha)$ values. If we consider the mathematical expression of $\mathcal{H}_n^{u'}(N_p|_\alpha)$, then

$$\mathcal{H}_n^{u'}(N_p|_\alpha) = \frac{\sum_{i=1}^{\mathcal{Z}|_\alpha} P\left(N_{p,i}^{\rm RS}\right) \ln\left[P\left(N_{p,i}^{\rm RS}\right)\right]}{\sum_{i=1}^{\mathcal{Z}|_{\alpha_{\rm RS}}} P(N_{p,i}) \ln[P(N_{p,i})]}, \tag{A1}$$

where $\mathcal{Z}|_\alpha$ ($\mathcal{Z}|_{\alpha_{\rm RS}}$) is the number of times the signal crosses α level ($\alpha_{\rm RS}$ level), we can clearly see the estimation of $\mathcal{H}_n^{u'}(N_p|_\alpha)$ is dependent on $\mathcal{Z}$. Our intuition suggests that as α increases, the number of level crossings would decrease given the rareness in the occurrences of large values in the signal. In Fig. 7(b), we plot the number of level crossings against $\alpha/\alpha_{\rm th}$ values. As one may note, $\mathcal{Z}$ values decrease beyond 1000 when the $\alpha_{\rm th}$ level is crossed. Since 1000 is a large number to ensure the estimates are statistically robust, we consider the $H_n^{u'}$ values to be 0.8. This can be further confirmed by plotting the cumulative distribution functions (CDFs) of event lengths. For visualization purposes, we only show the results corresponding to the u' signal at $y^+ = 66.84$. Quite

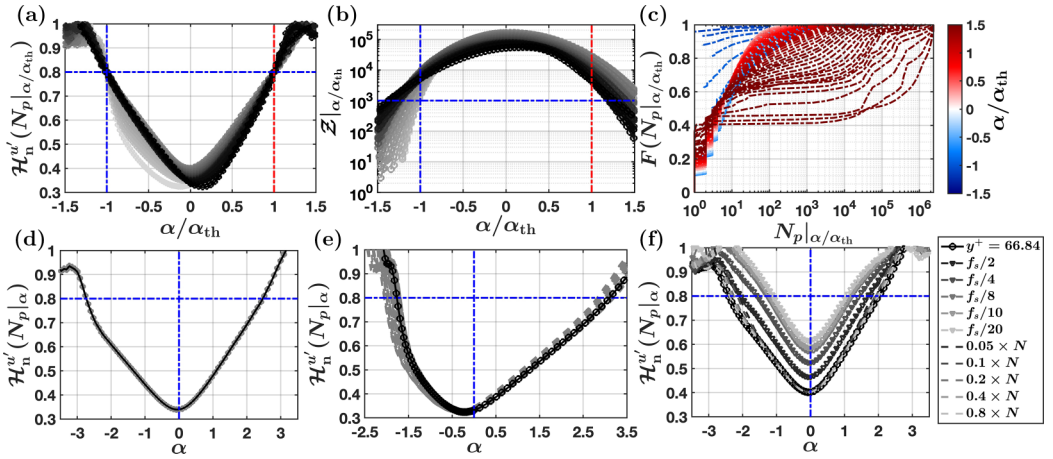

FIG. 7. (a) The Shannon entropy curves of event lengths are plotted with respect to the scaled threshold $\alpha/\alpha_{\rm th}$. This scaling ensures that the Shannon entropy curves converge towards the 0.8 value. (b) The number of zero crossings ($\mathcal{Z}$) are plotted against $\alpha/\alpha_{\rm th}$. The blue horizontal dash-dotted line indicates the number $\mathcal{Z} = 10^3$. (c) The cumulative distribution functions of the event lengths are shown for different levels of $\alpha/\alpha_{\rm th}$. (d) For $y^+ = 66.84$, the Shannon entropy curve of event lengths (black line) is compared with a randomly shuffled model of 50 realizations (gray shaded lines). (e) For $y^+ = 4.3$, the Shannon entropy curves are compared between individual ensembles of the measured time series (gray shaded lines) and the averaged one (black line). (f) The impacts of sampling frequencies (f_s) and the length of the time series (N) on the entropy curve are investigated by systematically varying f_s and N (see the legend).

clearly, the CDFs display abrupt jumps as α becomes larger than $\alpha_{\rm th}$, due to the lesser number of samples being used to compute their distributions [Fig. 7(c)].

It is important to take into account whether the entropy curves when compared with a RS signal change if different realizations of random sequences are used. We test this by generating 50 different realizations of RS sequences and compute the entropy curves for each of such realizations. In Fig. 7(d) we show such comparisons using u' signal at $y^+ = 66.84$ as the test case. No difference is noted in the results. Moreover, in the figures discussed in the main text, we show only the ensemble-averaged results by combining all the three measurement cycles over which the turbulent time series were collected at each y^+ value [27]. In Fig. 7(e), we compare the entropy curves for each ensemble member with the averaged one. We consider the u' signal at $y^+ = 4.3$ from the T1 dataset, since at this height the number of ensemble members remains the largest (120). It can be seen that the ensemble-averaged and individual entropy curves almost overlap with no major differences [Fig. 7(e)].

As a last measure, we investigate the influence of the length of the time series (N) and sampling frequencies (f_s) on the Shannon entropy curves. We artificially change the sampling frequencies by block averaging the u' signal values and by doing so we reduce the sampling frequencies as low as 0.05 times the original. Although the entropy curves do change under this operation, their overall shapes remain the same and therefore only appear as a scaled version of the original [Fig. 7(f)]. This change mainly occurs since by block averaging we alter the standard deviations of the signal and thus the α levels. Potentially it is also possible to increase the sampling frequencies by incorporating an interpolation model, namely piecewise cubic Hermite interpolating polynomial. By utilizing this model, we increase the sampling frequencies two and four times the original, and study its effects on the entropy curves. Similar as before, the curves preserve their shapes and scale according to the f_s values (not shown). On the other hand, if we sub-sample the time series at different lengths compared to the original, then $H_n^{u'}$ remains nearly the same even when sub-sampling reduces the original signal length by 95% [Fig. 7(f)]. Hence, we conclude that the estimation of the Shannon

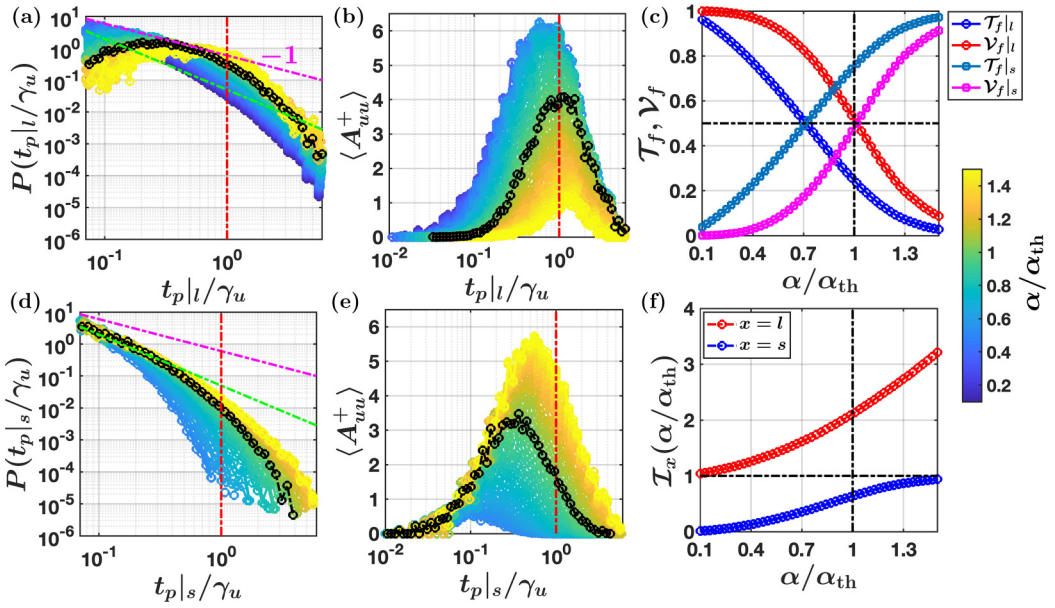

FIG. 8. For the l- and s-type events, [(a) and (d)] PDFs of timescales ($P(t_p|_x/\gamma_u$, where $x = \text{l, s}$) and the event amplitude ($\langle A^+_{uu}\rangle$) curves [(b) and (e)] are shown, with systematically changing the $\alpha/\alpha_{\rm th}$ values (see the color bar). The thick black lines denote the curves at $\alpha/\alpha_{\rm th} = 1$. The pink and green dash-dotted lines indicate power laws of slope -1 and -1.6, respectively, and the red lines indicate the location where the timescales ($t_p|_x$) equal to γ_u. (c) Fractional contributions of l-type or s-type events to the variance ($\mathcal{V}_f$) and occupation time ($\mathcal{T}_f$) are shown for various $\alpha/\alpha_{\rm th}$ values. The vertical and horizontal black lines indicate $\alpha/\alpha_{\rm th} = 1$ and $\mathcal{T}_f, \mathcal{V}_f = 0.5$. (f) The intermittency coefficient ($\mathcal{I}$) corresponding to l- and s-type events are shown against $\alpha/\alpha_{\rm th}$.

entropy curves are statistically robust, placing confidence in the computed α values used later to detect coherent structures.

APPENDIX B: EFFECTS OF α ON EVENT STATISTICS

Although while demarcating between the l- and s-type events we used $\alpha_{\rm th}$, it is possible to do the same with any α values. For instance, if the α values are chosen to be very small then nearly all the positive and negative events satisfy the condition of the l-type events, and therefore, they become almost indistinguishable from the unconditioned ones (i.e., the original zero-crossing events). Conversely, if the α values are too large, then the number of l-type events decrease substantially and overshadowed by the s-type events. It is thus interesting to consider how the statistics of l- and s-type events change when the α values are varied systematically, since this illustrates how sensitive the results are in Fig. 5 if one had used a different $\alpha_{\rm th}$ value to separate the events.

Instead of using all the signals from the T1 dataset, we carry out this sensitivity exercise for one particular u' signal. Precisely, for the same u' signal as used in Fig. 4 (i.e., at $y^+ = 66.84$), in Figs. 8(a) and 8(d), we show how the PDFs of $t_p|_l/\gamma_u$ and $t_p|_s/\gamma_u$ change as α is varied. Note that the different α values are scaled with respect to $\alpha_{\rm th}$, which is the original value used in Fig. 4 to separate the l- and s-type events. Specific to the l-type events, the PDFs at small α values are equivalent to the zero-crossing PDFs of u' signal, but as α increases the power-law exponent changes gradually from -1.6 to -1, with eventually attaining a log-normal distribution. On the other hand, the s-type events approach the zero-crossing PDFs at larger α values, notwithstanding their evolution remains

very different from the l-type ones. In particular, the distributions of $t_p|_s/\gamma_u$ differ significantly from $t_p|_l/\gamma_u$.

By turning our attention towards event contributions, one can see that with increasing α values the $\langle A^+_{uu}\rangle$ curves of l-type events attain their peaks at scales considerably larger than the integral scales [Fig. 8(b)]. By contrast, the peaks of the $\langle A^+_{uu}\rangle$ curves corresponding to s-type events are always smaller than the integral scales [Fig. 8(e)]. In fact, for small α values, their peaks occur at scales significantly lesser than γ_u. Therefore, it is plausible that by choosing an appropriate α one might separate the features of small-scale turbulence by conditionally sampling only the s-type events. This is, however, a topic for further research.

By integrating $\langle A_{uu}\rangle$ curves over all the possible timescales and dividing by the velocity variance, yields fractional contribution to σ_u^2 ($\mathcal{V}_f$) for either of the event types. Similarly, by summing up all the possible timescales and dividing by T, yields the occupation time fractions of l- and s-type events ($\mathcal{T}_f$). In Fig. 8(c), we show how $\mathcal{T}_f$ and $\mathcal{V}_f$ vary for the l-type and s-type events against $\alpha/\alpha_{\text{th}}$. At α_{th} level, we see that the l-type events nearly contribute 50% to the velocity variance while occupying 20% of the time. On the other hand, s-type events occupy 80% of the time while contributing the same to σ_u^2. This information can also be studied in terms of an intermittency index ($\mathcal{I}$), defined as a ratio between $\mathcal{V}_f$ and $\mathcal{T}_f$.

If $\mathcal{I}$ values are further scaled with the ones obtained from the unconditioned events ($\mathcal{I}_f$), then $\mathcal{I}_f \to 1$ when α is either too large or small, depending on s- or l-type events respectively. When $\mathcal{I}_f$ is plotted against $\alpha/\alpha_{\text{th}}$, a clear demarcation is noticed between l- and s-type events in how they approach the unit values [Fig. 8(f)]. We hypothesize this asymmetrical progression is related to the time-irreversible dynamics of wall-bounded flows [52]. An important point to note from Fig. 8 is, the event contribution curves, the timescale PDFs, and the fractional contributions corresponding to l- and s-type events do not change significantly when $\alpha/\alpha_{\text{th}}$ values are in and around unity, for instance between 0.8 to 1.2. Therefore, this indicates that the observations in Fig. 5 are fairly robust if the original α_{th} values were changed by around $\pm 20\%$.

APPENDIX C: SIGN-INDEFINITE VELOCITY SIGNAL

Some earlier studies used thresholds on the time-series values to detect coherent structures and suggested that the same could be applied interchangeably on either the original or absolute values of the signal [78]. We, however, show that considering absolute values of the velocity signals instead of the original affects how the events are organized in the temporal space.

To begin with, we show how the Shannon entropy curves of the event lengths would behave when the α levels are applied on the absolute values of the u' signal [Fig. 9(a)]. Note that it is not possible to set $\alpha = 0$ in case of absolute values since no crossings would be obtained in that case. Therefore, the smallest α levels are chosen as slightly larger than 0. By doing so, one observes that up to certain α values the vertical profiles of $H_n^{|u'|}(N_p|_\alpha)$ behave identically as $H_n^{u'}(N_p|_\alpha)$ in Fig. 2(a), when α is approached from the positive side. In fact, similar to $H_n^{u'}(N_p|_\alpha)$, an inflection point in $H_n^{|u'|}(N_p|_\alpha)$ is observed at $y^+ = 70$.

A note is necessary here regarding the estimation of the critical α value (α_{th}) for the $|u'|$ signal. The scaled entropy curves of $|u'|$ signals form an U shape, and because of that the 0.8 value can be reached either at small or large α levels [Fig. 9(b)]. At small α levels, the events have large timescales for the absolute signal, since the number of crossings are limited. However, we choose the critical α levels (α_{th}) from the larger side, in accordance with the original signal.

However, the biggest difference between the original and absolute signal occurs when one compares the mean timescales with the phase-randomized (PR) surrogates. Unlike u', for the absolute signals, $R|_{\alpha/\alpha_{\text{th}}}$ stays almost near to unity for any $\alpha/\alpha_{\text{th}}$ values [Fig. 9(c)]. This indicates, contrary to Fig. 6(e), the effect of nonlinear dynamics on the temporal arrangement of the samples exceeding α_{th} disappears by taking the absolute values. We can further confirm this phenomenon by comparing the vertical profiles of T_{th}/γ_u between u' and $|u'|$ signals.

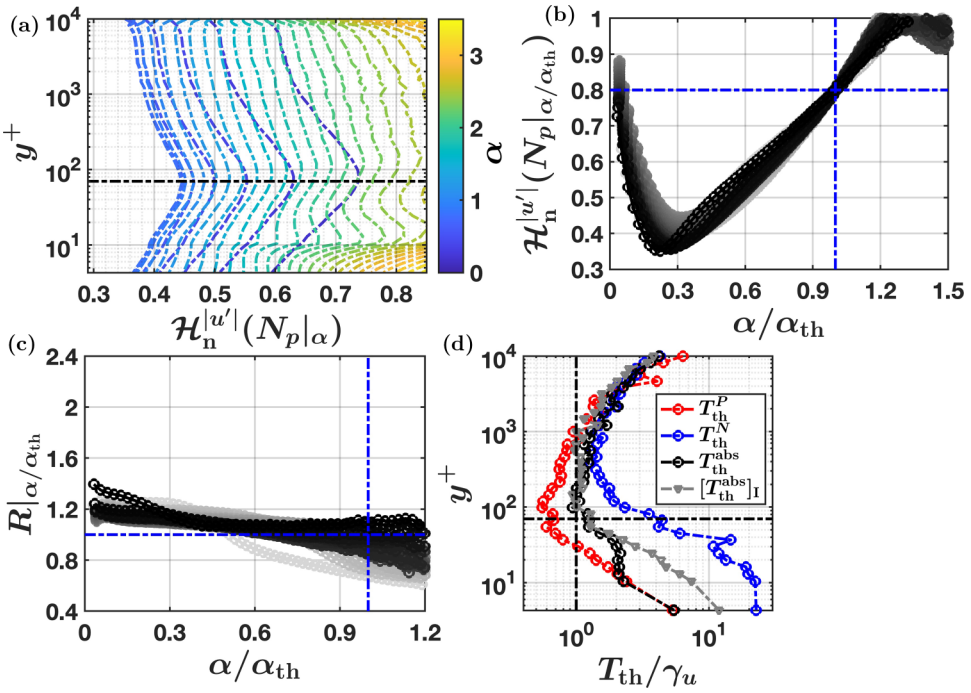

FIG. 9. (a) Vertical profiles of the Shannon entropy curves for the absolute values of the u' signals ($|u'|$) at different α levels are shown for the T1 dataset. (b) $\mathcal{H}_n^{|u'|}(N_p|_\alpha)$ values are plotted for different y^+ values, and α_{th} is identified where $\mathcal{H}_n^{|u'|}(N_p|_\alpha) = 0.8$. (c) The mean level-crossing timescales at different α/α_{th} levels are compared with a phase-randomized signal, where $R|_{\alpha/\alpha_{th}}$ denotes the ratios between the two. (d) The mean timescale computed at α_{th} level (T_{th}) are compared between the original and absolute values of the u' signals.

For $|u'|$, the mean timescales at α_{th} level remain closer to T_{th}^P instead of T_{th}^N, where T_{th}^P and T_{th}^N values are obtained from the original u' signal [Fig. 9(d)]. More importantly, T_{th} of the absolute signal is nearly insensitive when the Fourier phases are randomized. Since PR destroys the organization of coherent structures, this indifference suggests that the events detected from the absolute signals may not obey the turbulent flow physics.

[1] A. F. Hussain, Coherent structures—Reality and myth, Phys. Fluids **26**, 2816 (1983).
[2] D. Kaftori, G. Hetsroni, and S. Banerjee, Particle behavior in the turbulent boundary layer. I. Motion, deposition, and entrainment, Phys. Fluids **7**, 1095 (1995).
[3] K. C. Kim and R. J. Adrian, Very large-scale motion in the outer layer, Phys. Fluids **11**, 417 (1999).
[4] V. Nikora, R. Nokes, W. Veale, M. Davidson, and G. Jirka, Large-scale turbulent structure of uniform shallow free-surface flows, Environ. Fluid Mech. **7**, 159 (2007).
[5] A. Majda and P. Kramer, Simplified models for turbulent diffusion: Theory, numerical modelling, and physical phenomena, Phys. Rep. **314**, 237 (1999).
[6] M. Wan, S. Oughton, S. Servidio, and W. H. Matthaeus, Generation of non-Gaussian statistics and coherent structures in ideal magnetohydrodynamics, Phys. Plasmas **16**, 080703 (2009).
[7] C. Feigenwinter and R. Vogt, Detection and analysis of coherent structures in urban turbulence, Theor. Appl. Climatol. **81**, 219 (2005).
[8] J. Jiménez, Coherent structures in wall-bounded turbulence, J. Fluid Mech. **842**, P1 (2018).

[9] A. C.-L. Chian, E. L. Rempel, G. Aulanier, B. Schmieder, S. C. Shadden, B. T. Welsch, and A. R. Yeates, Detection of coherent structures in photospheric turbulent flows, Astrophys. J. **786**, 51 (2014).
[10] R. J. Adrian, Hairpin vortex organization in wall turbulence, Phys. Fluids **19**, 041301 (2007).
[11] G. S. Young, D. A. Kristovich, M. R. Hjelmfelt, and R. C. Foster, Rolls, streets, waves, and more: A review of quasi-two-dimensional structures in the atmospheric boundary layer, Bull. Am. Meteorol. Soc. **83**, 1001 (2002).
[12] I. Marusic, D. Chandran, A. Rouhi, M. K. Fu, D. Wine, B. Holloway, D. Chung, and A. J. Smits, An energy-efficient pathway to turbulent drag reduction, Nat. Commun. **12**, 5805 (2021).
[13] S. T. Salesky and W. Anderson, Coherent structures modulate atmospheric surface layer flux-gradient relationships, Phys. Rev. Lett. **125**, 124501 (2020).
[14] J. Weiss, A tutorial on the proper orthogonal decomposition, in *AIAA Aviation 2019 Forum* (AIAA, Reston, VA, 2019), p. 3333.
[15] A. Lozano-Durán, O. Flores, and J. Jiménez, The three-dimensional structure of momentum transfer in turbulent channels, J. Fluid Mech. **694**, 100 (2012).
[16] S. Dong, A. Lozano-Durán, A. Sekimoto, and J. Jiménez, Coherent structures in statistically stationary homogeneous shear turbulence, J. Fluid Mech. **816**, 167 (2017).
[17] A. Perry and C. Abell, Asymptotic similarity of turbulence structures in smooth-and rough-walled pipes, J. Fluid Mech. **79**, 785 (1977).
[18] A. Perry and M. Chong, On the mechanism of wall turbulence, J. Fluid Mech. **119**, 173 (1982).
[19] A. Perry and J. D. Li, Experimental support for the attached-eddy hypothesis in zero-pressure-gradient turbulent boundary layers, J. Fluid Mech. **218**, 405 (1990).
[20] M. R. Raupach, R. A. Antonia, and S. Rajagopalan, Rough-wall turbulent boundary layers, Appl. Mech. Rev. **44**, 1 (1991).
[21] A. J. Smits, B. J. McKeon, and I. Marusic, High–reynolds number wall turbulence, Annu. Rev. Fluid Mech. **43**, 353 (2011).
[22] B. Balakumar and R. Adrian, Large-and very-large-scale motions in channel and boundary-layer flows, Phil. Trans. R. Soc. A **365**, 665 (2007).
[23] R. Mathis, N. Hutchins, and I. Marusic, Large-scale amplitude modulation of the small-scale structures in turbulent boundary layers, J. Fluid Mech. **628**, 311 (2009).
[24] J. F. Morrison, The interaction between inner and outer regions of turbulent wall-bounded flow, Phil. Trans. R. Soc. A **365**, 683 (2007).
[25] M. Guala, M. Metzger, and B. J. McKeon, Interactions within the turbulent boundary layer at high Reynolds number, J. Fluid Mech. **666**, 573 (2011).
[26] G. Pathikonda and K. T. Christensen, Investigation of inner-outer interactions in a turbulent boundary layer using high-speed particle image velocimetry, Phys. Rev. Fluids **4**, 034607 (2019).
[27] W. Baars, K. Talluru, N. Hutchins, and I. Marusic, Wavelet analysis of wall turbulence to study large-scale modulation of small scales, Exp. Fluids **56**, 188 (2015).
[28] R. Antonia, Conditional sampling in turbulence measurement, Annu. Rev. Fluid Mech. **13**, 131 (1981).
[29] K. N. Rao, R. Narasimha, and M. B. Narayanan, The bursting phenomenon in a turbulent boundary layer, J. Fluid Mech. **48**, 339 (1971).
[30] P. H. Alfredsson and A. V. Johansson, Time scales in turbulent channel flow, Phys. Fluids **27**, 1974 (1984).
[31] M. Metzger, B. McKeon, and E. Arce-Larreta, Scaling the characteristic time of the bursting process in the turbulent boundary layer, Physica D **239**, 1296 (2010).
[32] C. Subramanian, S. Rajagopalan, R. Antonia, and A. Chambers, Comparison of conditional sampling and averaging techniques in a turbulent boundary layer, J. Fluid Mech. **123**, 335 (1982).
[33] G. Alfonsi, Coherent structures of turbulence: Methods of eduction and results, Appl. Mech. Rev. **59**, 307 (2006).
[34] S. Tardu and F. Bauer, Level-crossing statistics and production in low Reynolds number wall turbulence, J. Turbul. **16**, 847 (2015).
[35] D. Poggi and G. Katul, Evaluation of the turbulent kinetic energy dissipation rate inside canopies by zero-and level-crossing density methods, Bound.-Layer Meteorol. **136**, 219 (2010).

[36] I. Blake and W. Lindsey, Level-crossing problems for random processes, IEEE Trans. Inf. Theory **19**, 295 (1973).
[37] R. Friedrich, J. Peinke, M. Sahimi, and M. R. R. Tabar, Approaching complexity by stochastic methods: From biological systems to turbulence, Phys. Rep. **506**, 87 (2011).
[38] S. N. Majumdar, Persistence in nonequilibrium systems, Curr. Sci. **77**, 370 (1999).
[39] P. Perlekar, S. S. Ray, D. Mitra, and R. Pandit, Persistence problem in two-dimensional fluid turbulence, Phys. Rev. Lett. **106**, 054501 (2011).
[40] S. Chowdhuri, T. Kalmár-Nagy, and T. Banerjee, Persistence analysis of velocity and temperature fluctuations in convective surface layer turbulence, Phys. Fluids **32**, 076601 (2020).
[41] M. Heisel, C. M. de Silva, G. G. Katul, and M. Chamecki, Self-similar geometries within the inertial subrange of scales in boundary layer turbulence, J. Fluid Mech. **942**, A33 (2022).
[42] D. Cava, G. Katul, A. Molini, and C. Elefante, The role of surface characteristics on intermittency and zero-crossing properties of atmospheric turbulence, J. Geophys. Res. **117**, 2011JD016167 (2012).
[43] D. Li, G. G. Katul, and E. Bou-Zeid, Mean velocity and temperature profiles in a sheared diabatic turbulent boundary layer, Phys. Fluids **24**, 105105 (2012).
[44] G. Lancaster, D. Iatsenko, A. Pidde, V. Ticcinelli, and A. Stefanovska, Surrogate data for hypothesis testing of physical systems, Phys. Rep. **748**, 1 (2018).
[45] W. J. Baars, N. Hutchins, and I. Marusic, Self-similarity of wall-attached turbulence in boundary layers, J. Fluid Mech. **823**, R2 (2017).
[46] R. Deshpande, J. P. Monty, and I. Marusic, Streamwise inclination angle of large wall-attached structures in turbulent boundary layers, J. Fluid Mech. **877**, R4 (2019).
[47] C. J. Keylock, S. N. Lane, and K. S. Richards, Quadrant/octant sequencing and the role of coherent structures in bed load sediment entrainment, J. Geophys. Res. Earth. Surf. **119**, 264 (2014).
[48] C. J. Keylock, Multifractal surrogate-data generation algorithm that preserves pointwise Hölder regularity structure, with initial applications to turbulence, Phys. Rev. E **95**, 032123 (2017).
[49] C. J. Keylock, M. Ghisalberti, G. G. Katul, and H. M. Nepf, A joint velocity-intermittency analysis reveals similarity in the vertical structure of atmospheric and hydrospheric canopy turbulence, Environ. Fluid Mech. **20**, 77 (2020).
[50] I. Marusic, Two-point high Reynolds number zero-pressure gradient turbulent boundary layer dataset (2020), doi: 10.26188/5e919e62e0dac.
[51] G. Iacobello, L. Ridolfi, and S. Scarsoglio, Large-to-small scale frequency modulation analysis in wall-bounded turbulence via visibility networks, J. Fluid Mech. **918**, A13 (2021).
[52] G. Iacobello, S. Chowdhuri, L. Ridolfi, L. Rondoni, and S. Scarsoglio, Coherent structures at the origin of time irreversibility in wall turbulence, Commun. Phys. **6**, 91 (2023).
[53] See Supplemental Material at http://link.aps.org/supplemental/10.1103/PhysRevFluids.9.014601, we-compare the turbulence statistics, zero-crossing PDFs, level-crossing statistics, and structure functions between the two datasets.
[54] K. Sreenivasan and A. Bershadskii, Clustering properties in turbulent signals, J. Stat. Phys. **125**, 1141 (2006).
[55] M. Heisel, Effect of finite Reynolds number on self-similar crossing statistics and fractal measurements in turbulence, Phys. Rev. Fluids **7**, 014604 (2022).
[56] S. Chowdhuri, G. Iacobello, and T. Banerjee, Visibility network analysis of large-scale intermittency in convective surface layer turbulence, J. Fluid Mech. **925**, A38 (2021).
[57] M. I. Bogachev, J. F. Eichner, and A. Bunde, Effect of nonlinear correlations on the statistics of return intervals in multifractal data sets, Phys. Rev. Lett. **99**, 240601 (2007).
[58] P. Manshour, M. R. R. Tabar, and J. Peinke, Fully developed turbulence in the view of horizontal visibility graphs, J. Stat. Mech. **2015**, P08031 (2015).
[59] H. J. Bae and M. Lee, Life cycle of streaks in the buffer layer of wall-bounded turbulence, Phys. Rev. Fluids **6**, 064603 (2021).
[60] L. Wang, R. Hu, and X. Zheng, A scaling improved inner–outer decomposition of near-wall turbulent motions, Phys. Fluids **33**, 045120 (2021).

[61] R. Kinnison, *Applied Extreme-value Statistics*, Technical Report, Pacific Northwest National Laboratory, Richland, WA (1983).
[62] A. Comtet, P. Leboeuf, and S. N. Majumdar, Level density of a Bose gas and extreme value statistics, Phys. Rev. Lett. **98**, 070404 (2007).
[63] K. R. Sreenivasan and R. Antonia, The phenomenology of small-scale turbulence, Annu. Rev. Fluid Mech. **29**, 435 (1997).
[64] E. L. Crow and K. Shimizu, *Lognormal Distributions* (Marcel Dekker New York, 1987).
[65] A. Vela-Martín, The energy cascade as the origin of intense events in small-scale turbulence, J. Fluid Mech. **937**, A13 (2022).
[66] R. Deshpande, C. M. de Silva, and I. Marusic, Evidence that superstructures comprise self-similar coherent motions in high Reynolds number boundary layers, J. Fluid Mech. **969**, A10 (2023).
[67] Z. Harun and E. R. Lotfy, *Generation, Evolution, and Characterization of Turbulence Coherent Structures* (IntechOpen London, UK, 2018).
[68] J. L. Lumley, Coherent structures in turbulence, in *Transition and Turbulence* (Elsevier, Amsterdam, 1981), pp. 215–242.
[69] S. M. Tobias and F. Cattaneo, Limited role of spectra in dynamo theory: Coherent versus random dynamos, Phys. Rev. Lett. **101**, 125003 (2008).
[70] S. Duvvuri and B. J. McKeon, Triadic scale interactions in a turbulent boundary layer, J. Fluid Mech. **767**, R4 (2015).
[71] P. Schlatter and R. Örlü, Quantifying the interaction between large and small scales in wall-bounded turbulent flows: A note of caution, Phys. Fluids **22**, 051704 (2010).
[72] D. Poggi and G. Katul, Flume experiments on intermittency and zero-crossing properties of canopy turbulence, Phys. Fluids **21**, 065103 (2009).
[73] B. McKeon, The engine behind (wall) turbulence: Perspectives on scale interactions, J. Fluid Mech. **817**, P1 (2017).
[74] J. Hwang, J. Lee, H. J. Sung, and T. A. Zaki, Inner–outer interactions of large-scale structures in turbulent channel flow, J. Fluid Mech. **790**, 128 (2016).
[75] M. Guala, M. Metzger, and B. McKeon, Intermittency in the atmospheric surface layer: Unresolved or slowly varying? Physica D **239**, 1251 (2010).
[76] F. Liu, Z. Wu, P. Lv, W. Yang, and Y. Zhou, Evolution of the velocity gradient invariants in homogeneous isotropic turbulence with an inverse energy cascade, Phys. Fluids **35**, 025138 (2023).
[77] M. Heisel, T. Dasari, Y. Liu, J. Hong, F. Coletti, and M. Guala, The spatial structure of the logarithmic region in very-high-Reynolds-number rough wall turbulent boundary layers, J. Fluid Mech. **857**, 704 (2018).
[78] R. Narasimha, S. Kumar, A. Prabhu, and S. Kailas, Turbulent flux events in a nearly neutral atmospheric boundary layer, Phil. Trans. R. Soc. A **365**, 841 (2007).